Acta Oceanol. Sin., 2022, Vol. 41, No. 9, P. 149–157
https://doi.org/10.1007/s13131-022-1988-2
http://www.aosocean.com
E-mail: ocean2@hyxb.org.cn

Optical flow-based method to estimate internal wave parameters from X-band marine radar images

Jinghan Wen[1], Zhongbiao Chen[1], Yijun He[1, 2*]

[1] School of Marine Sciences, Nanjing University of Information Science & Technology, Nanjing 210044, China

[2] Key Laboratory of Space Ocean Remote Sensing and Applications, National Satellite Ocean Application Service, Beijing 100081, China

Received 5 August 2021; accepted 18 January 2022

Abstract

The velocity and direction of internal waves (IWs) are important parameters of the ocean, however, traditional observation methods can only obtain the average parameters of IWs for a single location or large area. Herein, a new method based on optical flow is proposed to derive the phase velocity vectors of IWs from X-band marine radar images. First, the X-band marine radar image sequence is averaged, and ramp correction is used to reduce the attenuation of gray values with increasing radial range. Second, the average propagation direction of the IWs is determined using the two-dimensional Fourier transform of the radar images; two radial profiles along this direction are selected from two adjacent radar images; and then, the average phase velocity of the IWs is estimated from these radial profiles. Third, the averaged radar images are processed via histogram equalization and binarization to reduce the influence of noise on the radar images. Fourth, a weighting factor is determined using the average phase velocity of a reference point; the phase velocities on the wave crest of the IWs are subsequently estimated via the optical flow method. Finally, the proposed method is validated using X-band marine radar image sequences observed on an oil platform in the South China Sea, and the error of the phase velocity is calculated to be 0.000 3–0.073 8 m/s. The application conditions of the proposed method are also discussed using two different types of IW packets.

Key words: internal wave, X-band marine radar, optical flow, phase velocity

Citation: Wen Jinghan, Chen Zhongbiao, He Yijun. 2022. Optical flow-based method to estimate internal wave parameters from X-band marine radar images. Acta Oceanologica Sinica, 41(9): 149–157, doi: 10.1007/s13131-022-1988-2

1 Introduction

Internal waves (IWs) are ubiquitous in the ocean and play important roles in energy transfer, biological processes, marine production activities, and ocean engineering. Because IWs frequently occur in the South China Sea (SCS), observing these waves in this region is highly significant (Huang et al., 2016).

In-situ observations, such as acoustic Doppler current profiles and conductivity–temperature–depth, are widely used to observe IWs. These strategies enable the observation of the amplitude, period, phase velocity, polarity, and other characteristics of IWs with high accuracy (Briscoe, 1975) but are usually limited to specific locations. Moreover, they cannot determine the characteristics of IWs at different locations.

Developments in satellite remote sensing have enabled the observation of IWs using optical and microwave satellite images. Synthetic aperture radar (SAR) can obtain high-resolution (several meters) sea surface images, rendering it suitable for observing IWs (Yang et al., 2001); additionally, it has the advantage of being able to conduct all-day, all-weather operations. Alpers (1985) presented a fundamental radar imaging theory of IWs for SAR in 1985, i.e., IW leads to sea-surface convergence or divergence, which changes the surface roughness, thereby affecting the gray level of the radar image. Many characteristics of IWs have been estimated in the literature based on this study, such as the velocity of IWs (Li et al., 2000), the characteristic half-widths of IWs (Zheng et al., 2001), the amplitudes of IWs (Jia et al., 2019), and the spatial distribution of IWs (Liu et al., 1998; Ning et al., 2020). The moderate resolution imaging spectroradiometer (MODIS) has a large swath area of several hundred kilometers, fine spatial resolution, and near-daily global coverage; hence, it is commonly used to study the IWs, in particular, to study characteristics such as the occurrence frequency (Jackson, 2007; Wang et al., 2011), propagation and sources (Sun et al., 2019; Wang et al., 2013), and spatial distribution (Zhou et al., 2016) of IWs.

X-band marine radar has high spatiotemporal resolution and can obtain sea surface images in real-time. Thus, this technology may help determine the evolution of an IW packet (Kropfli et al., 1999). The imaging mechanism of X-band marine radar is similar to that of SAR; specifically, it detects modulations in sea surface roughness associated with currents induced by IWs (Xue et al., 2013). Watson and Robinson (1990) studied the evolution of IWs in the Strait of Gibraltar using X-band marine radar images. Orr and Mignerey (2003) used X-band marine radar to track IWs in the SCS. Ramos et al. (2009) used Radon transform to calculate IW parameters, such as the propagation direction of IWs, their nonlinear velocity, the distance between solitary waves, and the number of solitary waves in each packet, from radar backscatter images. Lü et al. (2010) employed Radon transform to re-

Foundation item: The National Natural Science Foundation of China under contract Nos 41620104003 and 42027805; the National Natural Science Youth Foundation of China under contract No. 41506199.
*Corresponding author, E-mail: yjhe@nuist.edu.cn

trieve the propagation direction and velocity of IW packets in the northeastern SCS and then estimated the mixed layer depth by using the two-layer finite depth model. Plant et al. (2011) found at least two different types of IWs in the SCS by analyzing the images of shipborne dual-polarized coherent X-band radar deployed in the SCS. Pan and Jay (2009) used X-band radar images to track IW packets in the Colombia River and subsequently analyzed the characteristics of the detected IWs in combination with the KdV equation. Zha et al. (2012) used X-band radar images in combination with the Morison empirical formula to estimate the force exerted by IWs on a cylindrical pile. Lund et al. (2013) proposed an automated retrieval method of IWs from radar images and discussed the characteristics of IWs with amplitudes greater than 20 m. Badiey et al. (2016) estimated the speed, propagation direction, and amplitude of IWs by analyzing the data obtained from moored thermistor chains and an X-band radar.

Previous studies mostly estimated the average parameters of IWs, such as their average phase velocity and propagation direction (Ramos et al., 2009); unfortunately, these parameters cannot determine the phase velocity of different parts of the waves, which are important for studying the evolution of IWs. However, the distribution of IWs is complex as the latter may show significant changes over areas with a varied topography. Thus, obtaining the small-scale evolution of IWs using traditional methods is challenging. This study proposes a novel method to extract the phase velocity vector of each point on the crest of IWs using X-band marine radar images. The rest of this paper is organized as follows. Section 2 introduces the experimental data, Section 3 presents the method of extracting IW parameters from X-band radar images, and Section 4 verifies and discusses the method. Finally, the conclusions are presented in Section 5.

2 Data

An experiment was performed in September 2017 on an oil platform in the SCS. The observed sea area lies ~100 km south of Hainan Island (Fig. 1), where the IWs appear frequently (Liang et al., 2019; Jia et al., 2021). The water depth of the region is ~90 m, and the water depth gradually decreases from southeast to northwest. The tides in the observed sea area are mainly irregular diurnal tides. IWs often appear and propagate from southeast to northwest or from east to west (Wang et al., 2013). The X-band marine radar used in the experiment is developed based on a commercial Furuno Far-2127 shipborne navigation radar. Data

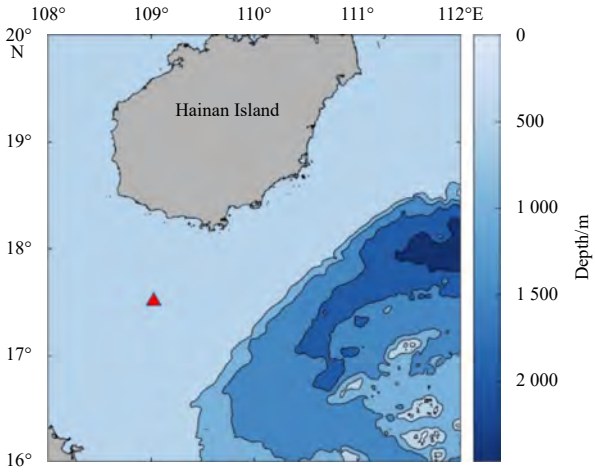

Fig. 1. Topographic map of the study region in the northern South China Sea. The red triangle marks the location of the radar station.

acquisition software is developed to convert the backscatter from the sea surface into an 8-bit gray value image (Chen et al., 2019). The main configurations of the radar are listed in Table 1. The antenna rotation speed is 42 r/min, and hence, the temporal resolution of the radar is 1.43 s. A single radar image sequence contains 32–128 radar images, and the time difference between two adjacent image sequences is 3–10 min. The radial resolution of the radar is 3.75 m, and the measurement ranges were ~6 km. As an example, Fig. 2 shows two images collected by the X-band

Table 1. Configuration of the X-band marine radar system

Parameter	Value
Polarization	HH
Radar frequency/MHz	9 410±30
Pulse width/ns	70
Pulse repetition frequency/Hz	3 000
Transmit power/kW	25
Beamwidth (3 dB)/(°)	~1 horizontally, ~20 vertically
Antenna	2.4 m slotted waveguide antenna
Antenna rotation speed/(r·min^{-1})	42
Sample frequency/MHz	40

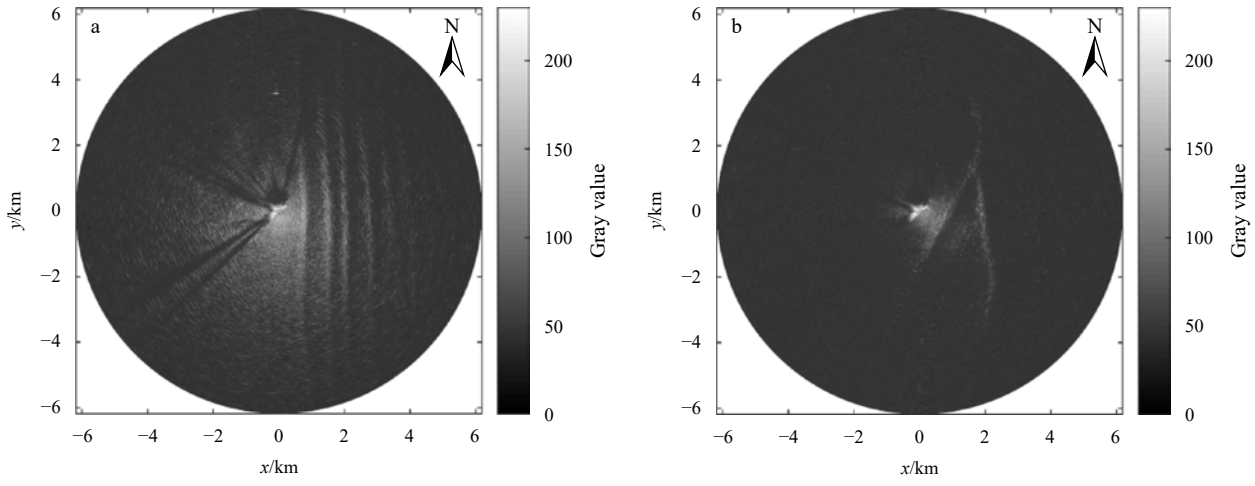

Fig. 2. Two X-band marine radar images obtained during the experiment. The images were recorded on September 1, 2017, at 23:15 UTC (a) and September 11, 2017, at 07:12 UTC (b).

radar when IWs pass; here, the wide adjacent bright and dark bands reflect radar echoes caused by changes in sea surface roughness due to IWs, and small wind waves are superimposed on the wide bands. The wave crests of the IW packet are regular in Fig. 2a but intersect in Fig. 2b. Thus, the variation of IWs in this area is complex.

Given the limitations of the experimental conditions, no *in-situ* measurement of IWs was conducted. Instead, synchronous MODIS images of the region were selected to verify the IWs recorded by the X-band marine radar images. The MODIS sensors are onboard the National Aeronautics and Space Administration's Earth Observing System satellites Terra and Aqua (Jackson, 2007). Terra and aqua transit at 10:30 (local time) and 13:30 (local time) every day. The MODIS has a swath width of 2 330 km and a spatial resolution of 250 m; it can be used to observe ocean IWs at a large scale. Because the optical satellite images are easily blocked by clouds, only two groups of matched X-band marine radar images and MODIS images were obtained.

3 Methodology

This section describes the method of extracting IW parameters from X-band marine radar images, including the phase velocities on the crests of the IWs, the number of solitary waves, and their distances in the IW packet.

3.1 *Data preprocessing*

3.1.1 *Averaging*

The radar image sequence is first averaged to reduce the influence of wind waves on the X-band marine radar images. For an X-band marine radar image sequence, $I(r,\varphi,t)$, I is the gray value of the radar image; r and φ are the radial distance and azimuthal angle from the radar, respectively; and t is the observation time. Each sequence of radar images is averaged over time, and the averaged radar image $\bar{I}(r,\varphi,t)$ is obtained.

Two adjacent radar image sequences must be selected, i.e., $\bar{I}_{c1}\left(r,\varphi_p,t_1\right)$ and $\bar{I}_{c2}\left(r,\varphi_p,t_2\right)$, where t_1 and t_2 are the average recording times of the two image sequences, to obtain the phase velocity vector of IWs. The two image sequences meet the following conditions: (1) the observation time between the two sequences is less than 5 min (i.e., $|t_1-t_2|<5$ min) and (2) each radar image sequence contains more than 32 images.

3.1.2 *Ramp correction*

The backscatter intensity of X-band radar decreases with increasing distance (Lund et al., 2013). Thus, removing the ramp of gray values with distance is necessary to extract the characteristics of IWs effectively.

The power function is used to fit the gray values of the averaged radar image for each φ_0 to obtain the dependence of radar backscatter image on the range,

$$\bar{I}_{fi}(r,\varphi_0,t)=a\cdot r^b \quad (i=1,2), \tag{1}$$

where a and b are coefficients that can be determined using the least-squares method.

The ramp of the radar images is then corrected as follows:

$$\bar{I}_{ci}(r,\varphi_0,t)=\bar{I}_i(r,\varphi_0,t)-\bar{I}_{fi}(r,\varphi_0,t) \quad (i=1,2). \tag{2}$$

Following radar backscatter ramp correction, the gray values of the radar image are adjusted to the range of 0–255 as follows:

$$\bar{I}_{ci}(r,\varphi,t)=\frac{\bar{I}_{ci}(r,\varphi,t)-\min\left(\bar{I}_{ci}(r,\varphi,t)\right)}{\max\left(\bar{I}_{ci}(r,\varphi,t)\right)-\min\left(\bar{I}_{ci}(r,\varphi,t)\right)}\times 255. \tag{3}$$

3.2 *Retrieval of the average parameters of IWs*

Two-dimensional fast Fourier transform (2D-FFT) is applied to the radar images to obtain the average propagation direction of the IWs. The 2D wavenumber spectrum of the IWs is then obtained. The average propagation direction of the IW packet can be obtained using

$$\varphi_p=\arctan\left(\frac{k_{y\max}}{k_{x\max}}\right), \tag{4}$$

where the wavenumbers $k_{x\max}$ and $k_{y\max}$ are the peak wavenumbers of the spectrum.

According to Eq. (4), the propagation direction of an IW has an ambiguity of 180°. Thus, cross-spectral analysis of the two adjacent radar images is used to determine the actual propagation direction of IWs (Chen et al., 2019).

The radar radial profiles at φ_p are selected. The number of ISWs in an IW packet can be obtained based on the number of peaks in a radial profile. The distance between adjacent ISWs in the IW packet can also be obtained based on the position of each wave peak in a radial profile. The phase velocity of each ISW can be estimated as

$$v_i=\frac{\Delta r_i}{\Delta t} \quad (i=1,2,\ldots), \tag{5}$$

where Δr_i is the distance difference between the ith ISW peak of the two radial profiles, and Δt is the time difference between two adjacent radar images.

Owing to the small observation range of X-band marine radar, a radar image may not cover all ISWs of an IW packet. Thus, the number of ISWs and the average phase velocity of the IW packet may have to be determined using multiple X-band radar image sequences.

3.3 *Determination of phase velocity vectors on an IW crest*

The optical flow method is widely used in moving-target tracking and dynamically analyzes images according to the characteristics of each pixel (Horn and Schunck, 1981). It is used herein to track IWs and extract the phase velocity vector on different locations of the IW. In this method, the gray value of the image before and after motion remains unchanged as a prerequisite,

$$\frac{\mathrm{d}\bar{I}}{\mathrm{d}t}=0. \tag{6}$$

Using the chain rule for differentiation, we find that the equation of optical flow for a gray image observed by X-band marine radar is

$$\bar{I}_x u+\bar{I}_y v+\bar{I}_t=0, \tag{7}$$

where $\bar{I}_x=\frac{\partial\bar{I}}{\partial x}$, $\bar{I}_y=\frac{\partial\bar{I}}{\partial y}$, and $\bar{I}_t=\frac{\partial\bar{I}}{\partial t}$ represent the partial derivatives of the averaged gray value and $u=\frac{\mathrm{d}x}{\mathrm{d}t}$, $v=\frac{\mathrm{d}y}{\mathrm{d}t}$ represent the propagation velocity, i.e., optical flow, of the pixels along the

x and y directions, respectively. As Eq. (7) has two unknowns u and v, to solve the problem, the Horn–Schunck algorithm adds another constraint, the smoothness constraint, which assumes smoothness in the flow over the whole image; thus, it tries to minimize distortions in flow and prefers solutions that show more smoothness. Then, combined with Eq. (7), the Horn–Schunck algorithm reduces the optical flow solution to the following extreme value problem (Gong and Bansmer, 2015),

$$E_{rr}{}^2 = \iint \left[\left(I_x u + I_y v + I_t \right)^2 + \lambda \left(u_x^2 + u_y^2 + v_x^2 + v_y^2 \right) \right] \mathrm{d}x\mathrm{d}y, \quad (8)$$

which is usually replaced by the following equation in practice,

$$E_{rr}{}^2 = \iint \left[\left(I_x u + I_y v + I_t \right)^2 + \lambda \left((u-\bar{u})^2 + (v-\bar{v})^2 \right) \right] \mathrm{d}x\mathrm{d}y, \quad (9)$$

where λ is an unknown weighting factor because the value of it needs to consider the noise in the X-band radar image. Solving this extreme problem, we can determine the velocity of each point in the image as follows:

$$\begin{cases} u^{n+1} = \bar{u}^n - \bar{I}_x \dfrac{\bar{I}_x \bar{u}^n + \bar{I}_y \bar{v}^n + \bar{I}_t}{\lambda^2 + \bar{I}_x^2 + \bar{I}_y^2}, \\ v^{n+1} = \bar{v}^n - \bar{I}_y \dfrac{\bar{I}_x \bar{u}^n + \bar{I}_y \bar{v}^n + \bar{I}_t}{\lambda^2 + \bar{I}_x^2 + \bar{I}_y^2}. \end{cases} \quad (10)$$

The average phase velocity (Eq. (5)) estimated from the radial profiles at φ_p is selected to determine λ according to the following steps.

First, the two adjacent radar images $\bar{I}_{c1}(r, \varphi, t_1)$ and $\bar{I}_{c2}(r, \varphi, t_2)$ are processed via histogram equalization and then converted into binary images to obtain the stripes of IWs. To reduce the influence of noise, regions with less than 50 pixels in the binary image are removed.

Second, the phase velocity of each ISW in the wave packet is estimated using the method described in Section 3.2, and the average phase velocity of the IW is used as the reference phase velocity. For convenience, each peak in the radial profile at φ_p is considered a reference point.

Third, the weighting factor is set to change from λ_1 to λ_2 and then used to estimate the phase velocity of each point in the image (Eq. (10)). Thus, the phase velocities near the reference points can be determined for different λ. The weighting factor λ_0 is selected to be that in which the phase velocity is closest to the phase velocity of the reference point. Finally, the phase velocity of each point in the radar image can be obtained by applying λ_0, as shown in Eq. (10).

The method to estimate IW parameters from X-band marine radar images is shown in Fig. 3.

4 Results and discussion

Different types of IW images observed by X-band radar (i.e., a set of single IW packet and a set of crossed ISWs) are used to estimate the IW parameters and verify the proposed method for re-

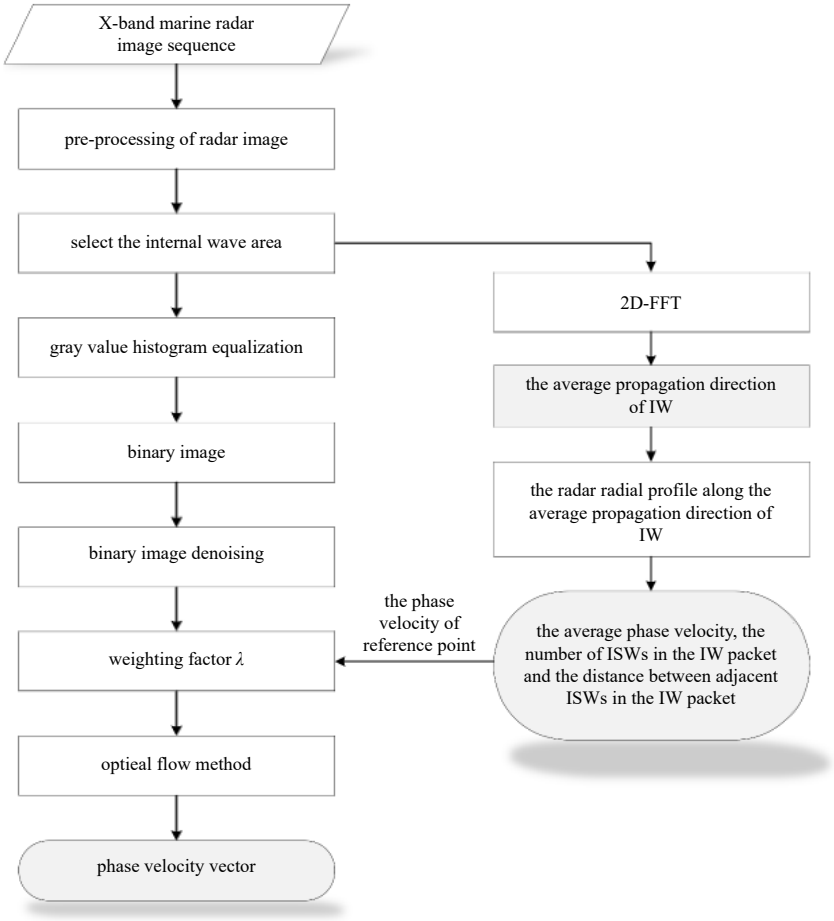

Fig. 3. Retrieval of internal wave (IW) parameters for X-band marine radar images.

trieving IW parameters from X-band radar images. Because *in-situ* measurements are not conducted in the experiment, the MODIS images are used to verify the distribution of IWs. The phase velocities estimated by the proposed optical flow-based method are verified using the average phase velocity of the reference point.

4.1 *Single IW packet*

A MODIS image acquired on September 2, 2017, at 03:30 UTC is shown in Fig. 4; in the figure, multiple groups of IW packets may be observed. A group of IW packets located approximately 9.1 km to the west of the radar station could be observed to propagate from east to west. According to the empirical formula in (Tang, 2019), the phase velocity of IWs in the region is approximately 0.76 m/s. Thus, the IW packets would arrive at the radar at ~00:10 UTC on September 1, 2017. The X-band radar image sequence recorded on September 1, 2017, at 23:15 UTC matches the IW in the MODIS image. As shown in Fig. 2a, the propagation direction of the IW packet in the X-band radar image agrees with that determined from the MODIS image (Fig. 4), i.e., the stripes in the X-band marine radar image sequence reflect the IW packet observed by MODIS.

The X-band radar image sequence is averaged using the method described in Section 3.1.1, as shown in Fig. 5. Average processing smoothens the wind waves and swells in the image, thereby facilitating the identification of IW stripes.

The gray values are fitted with the distance determined by the radar by using Eq. (1) to perform ramp correction on the radar image. Figure 6 shows a fitting curve of this group of images. The R-squared value of the fitting results is 0.999 3, which means the selected power function model is applicable to the present case.

The 2D wavenumber spectrum is obtained via 2D FFT of the radar image in the study area (Fig. 7). The propagation direction of the IW in Fig. 7 can be calculated as 90° or 270° (Eq. (4)), and the actual propagation direction of the IW packet can be determined. Cross-spectral analysis reveals that the IW packet propagates from east to west, as shown by the red dashed line in Fig. 7.

After determining the propagation direction of the IW, the radial profiles of the two adjacent radar image sequences are selected at the azimuth of this direction, as shown in Fig. 8. The IW packet contains four ISWs, the distances between which are 219 m, 158 m, and 227 m. The phase velocities at each reference point of the IW packet are 1.01 m/s (leading wave), 1.09 m/s, 1.14 m/s, and 1.18 m/s (Eq. (5)). Typically, the leading wave in an IW packet shows the maximum amplitude; thus, the backscatter intensity caused by the leading wave is largest in the radar image while those caused by the latter ISWs gradually decrease, consistent with the changes in the gray values in Fig. 8.

Histogram equalization is then applied to the two average adjacent radar images (Fig. 9a) to reduce the attenuation of gray values with the range. The images are converted into binary images by selecting a threshold gray value (Fig. 9b), and regions with less than 50 pixels are removed from the binary images (Fig. 9c) to enhance the extraction of IW information.

The value of λ_0 can be determined according to the velocity at the reference point in Fig. 7, and the phase velocity at each point of the IW crest can be obtained using the optical flow-based method (Eq. (10)), as shown in Fig. 10. Therein, the directions of the points on the IW crest line are perpendicular to the crest line. The phase velocities estimated by different methods are listed in Table 2. The phase velocities of ISWs estimated using the optical flow-based method range from 1.06 m/s to 1.11 m/s, which agrees with the velocities of the IWs determined in this area in previous studies (Orr and Mignerey, 2003; Liang et al., 2019; Tang, 2019); thus, the IW phase velocity estimated by the optical flow-based method is reasonable. The error of reference points A3 and A4 is 0.07–0.08 m/s, which is mainly due to the attenuation of radar backscatter with increasing range.

4.2 *Crossed ISWs*

The MODIS image obtained on September 11, 2017, at 03:24 UTC is shown in Fig. 11. Two groups of IW packets may be observed at ~13 km to the east and southeast of the radar station, and these packets propagate from east to west and from southeast to northwest, respectively. According to the empirical formula proposed by Tang (2019), the IW packet will arrive at the

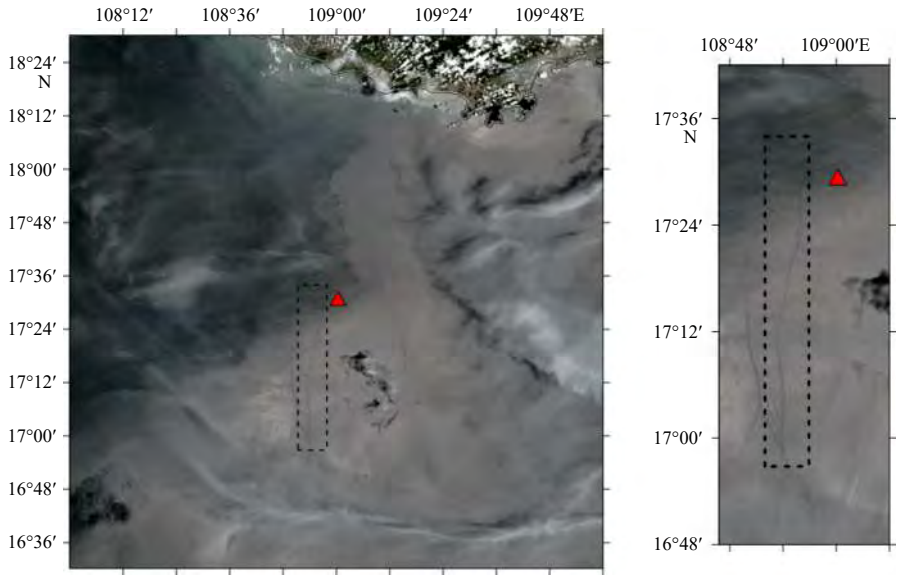

Fig. 4. MODIS image obtained on September 2, 2017, at 03:30 UTC. The red triangle marks the location of the X-band marine radar, and the black dash box shows an IW packet propagating from east to west. The right image shows the enlarged image close to the radar station.

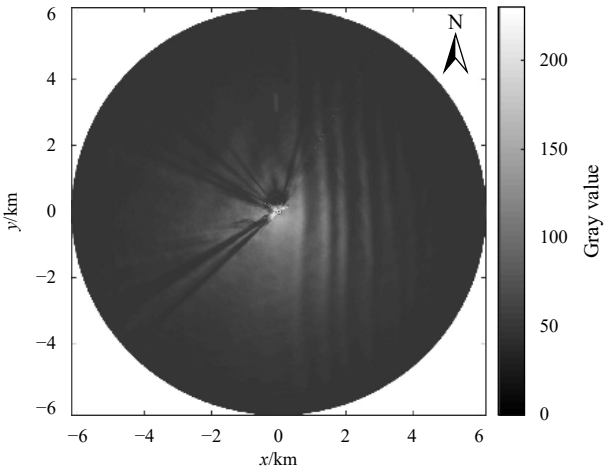

Fig. 5. Averaged image of a set of X-band radar image sequences recorded on September 1, 2017, at 23:15 UTC.

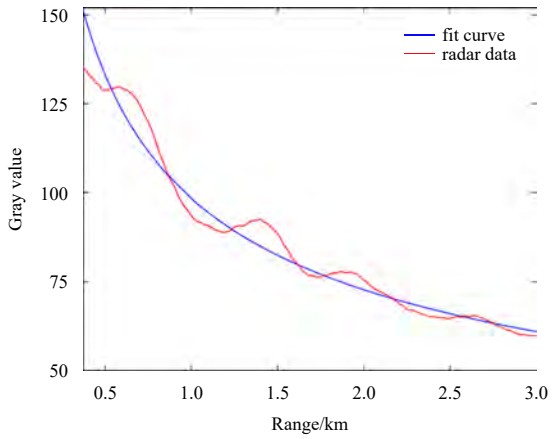

Fig. 6. Variations in gray value as a function of range.

radar station at ~08:09 UTC on September 11, 2017. The matched X-band radar image sequence was recorded on September 11, 2017, at 07:12 UTC, as shown in Fig. 2b, and the propagation directions of the two IW packets detected agree with those shown in

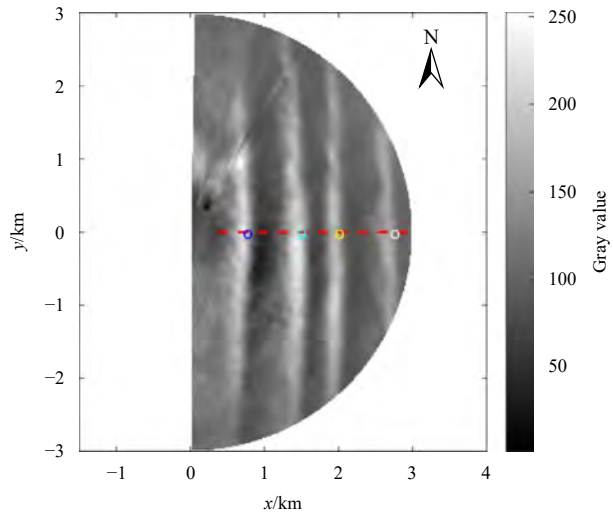

Fig. 7. Preprocessed radar image recorded on September 1, 2017, at 23:15 UTC. The red dashed line shows the average direction, and the circles indicate the positions of the reference points (left to right: A1, A2, A3, and A4).

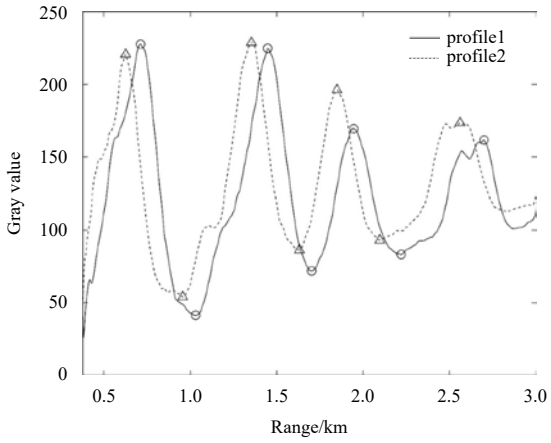

Fig. 8. Radial profiles of two adjacent radar image sequences. The IW propagates from right to left.

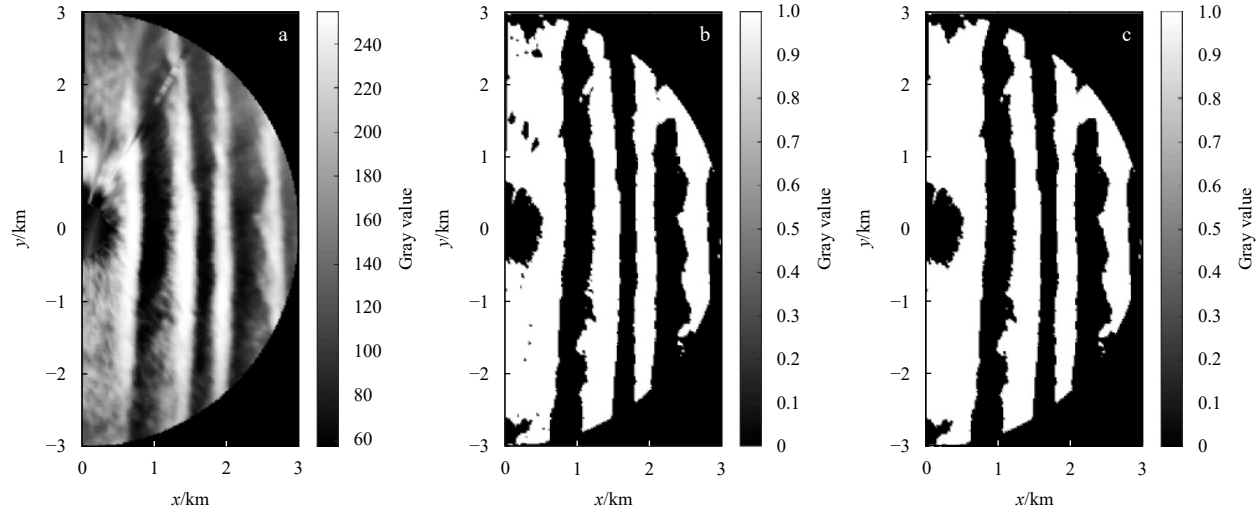

Fig. 9. Radar image processed via histogram equalization (a), binarization (b), and noise reduction (c).

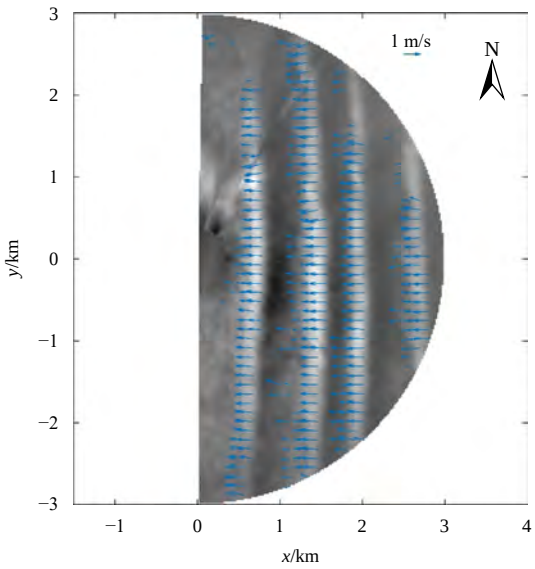

Fig. 10. Optical flow field estimated from X-band marine radar images. The arrows indicate the phase velocity vectors of the IW packet.

the MODIS image (Fig. 11). In other words, X-band marine radar correctly observed the two groups of IW packets.

The X-band radar image sequences are first preprocessed, after which 2D-FFT is used to obtain the IW wavenumber spectrum, which shows two main spectral peaks. The propagation directions of the two ISWs, which are $\varphi_{p_1}=300°$ and $\varphi_{p_2}=270°$, can be determined by cross-spectral analysis, as shown in Fig. 12.

The radial profiles $\bar{I}_{c1}\left(r,\varphi_{p_1}\right)$ and $\bar{I}_{c2}\left(r,\varphi_{p_1}\right)$ of two adjacent radar image sequences are selected in the propagation direction of the ISWs, as shown in Fig. 13. According to the locations of reference point B1 (Fig. 12, yellow circle), the phase velocity of this point is estimated to be 0.74 m/s using Eq. (5).

After the radar images are processed via histogram equalization and noise reduction, λ is determined using the phase velocity at reference point B1 to be λ_0 = 1.18. The phase velocities of the points on the IW crest are obtained by the optical flow-based method with the selected λ_0, as shown in Fig. 14.

Figure 14 shows that the proposed method could detect the propagation directions of the points on the crest of the IWs accurately and that the distribution of phase velocities is reasonable. Some errors in the region of approximately x=0.6 and y=1–2 km may be detected because noise cannot be completely eliminated from the image (Horn and Schunck, 1981). The phase velocity estimated by the optical flow-based method for reference point B2 is 1.15 m/s, which also agrees with the phase velocity of IWs in this region determined in previous studies (Orr and Mignerey, 2003; Liang et al., 2019; Tang, 2019). The phase velocities calculated using different methods are listed in Table 3.

Figures 10 and 14 clearly show that the proposed optical flow-based method is applicable not only to single IW packet with parallel ISWs but also to crossed IWs.

4.3 *Discussion on the selection of reference point*

In the proposed method, the determination of λ_0 is important. To study the sensitivity of the value to the method, the other reference point B2 (Fig. 12), has been chosen to determine the value of λ_0. The adjacent two radial profiles along the propagation direction of the ISW B2 are shown in Fig. 15. According to the radial profiles, the average phase velocity at point B2 is estimated to be 1.14 m/s, and the value of λ_0 is 1.19. Using the optical flow-based method, the phase velocities of the crossed IWs are estimated,

Table 2. Phase velocities estimated using different methods

	Radial profiles	Optical flow-based method	X-band radar (Orr and Mignerey, 2003)	SAR observations (Liang et al., 2019)	Empirical formula (Tang, 2019)
Reference point A2	1.09 m/s	1.11 m/s	1.17 m/s	0.89 m/s	0.76 m/s
Reference point A3	1.14 m/s	1.06 m/s	1.17 m/s	0.89 m/s	0.76 m/s
Reference point A4	1.18 m/s	1.11 m/s	1.17 m/s	0.89 m/s	0.76 m/s

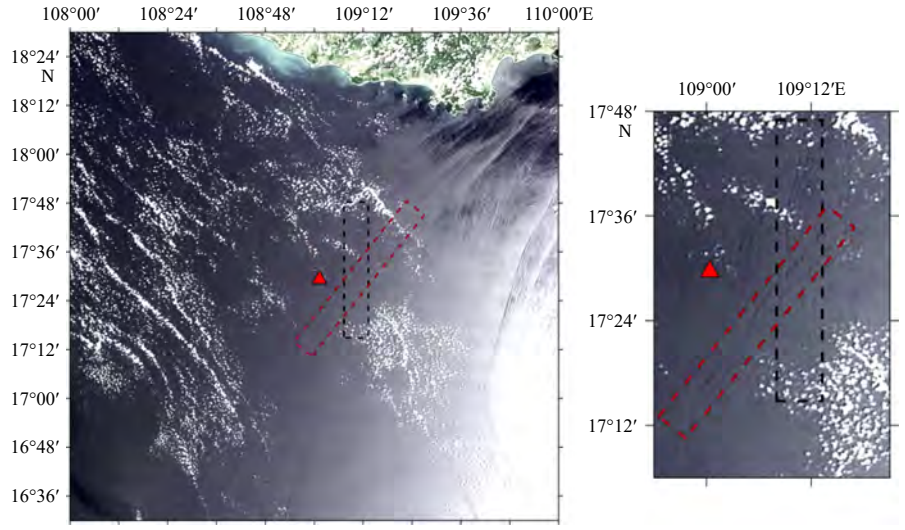

Fig. 11. MODIS image obtained on September 11, 2017, at 03:24 UTC. The red triangle marks the position of the radar station. The black box indicates the IW packet propagating from east to west, and the red box indicates the IW packet propagating from southeast to northwest. The right image shows the enlarged image that is close to the radar station.

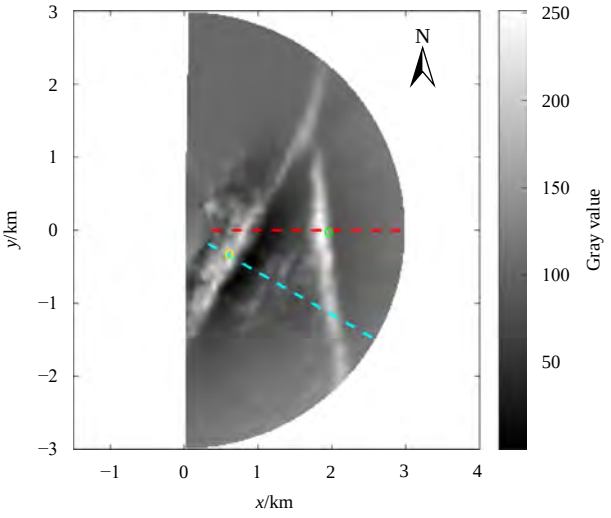

Fig. 12. Preprocessed radar images recorded on September 11, 2017, at 07:12 UTC. Here, the blue dash line indicates the propagation direction of the first ISW ($\varphi_{p_1}=300°$), and the red dash line indicates the propagation direction of the second ISW ($\varphi_{p_2}=270°$). The yellow circle indicates the position of reference point B1, and the green circle indicates the position of reference point B2.

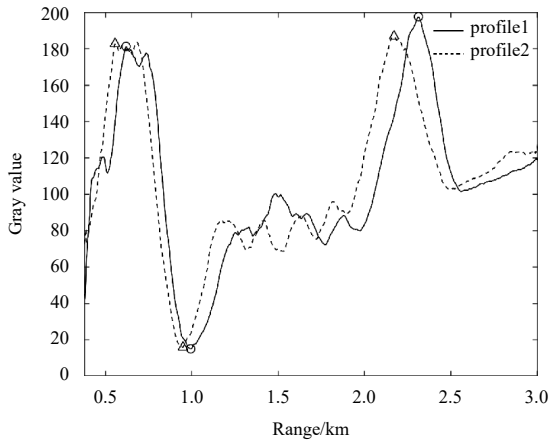

Fig. 13. Radial profiles of two adjacent radar image sequences in the propagation direction $\varphi_{p_1}=300°$ of ISWs.

and velocity at the reference point B1 is 0.73 m/s. Compared to the average phase velocity of B1 estimated from the adjacent radial profiles, the relative error of the phase velocity at B1 is 0.01 m/s. Therefore, the proposed method is affected little by the selection of different reference points, i.e., the optical flow-based method is stable.

5 Conclusions

Phase velocity is one of the most important parameters of IWs. Previous methods of extracting the phase velocity of ISWs mostly estimated the average phase velocity from satellite images. Although the observation range of X-band marine radar is smaller than that of satellite images, X-band marine radar can observe the sea surface in real-time and continuously, which is important for studying the evolution of IWs (Kropfli et al., 1999). Previous methods of extracting the phase velocity of ISWs from X-band radar images were mostly based on Radon transform,

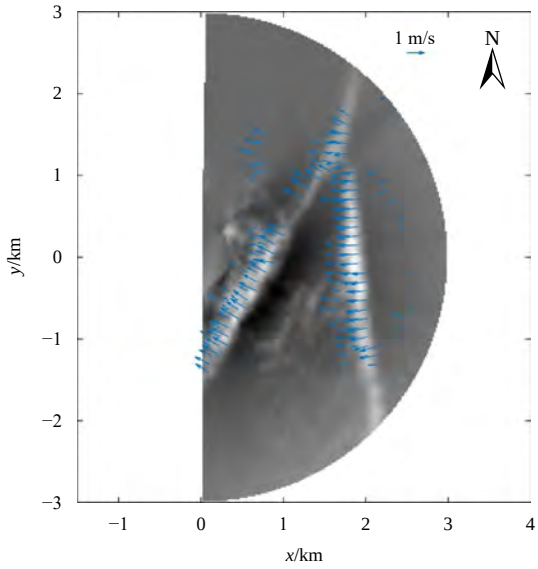

Fig. 14. Optical flow field estimated from X-band radar images. The arrows indicate the phase velocity vectors of IW packets.

Table 3. Phase velocities calculated using different methods

	Radial profiles	Optical flow-based method	X-band radar (Orr and Mignerey, 2003)	SAR observations (Liang et al., 2019)	Empirical formula (Tang, 2019)
Reference B2	1.14 m/s	1.15 m/s	1.17 m/s	0.89 m/s	0.76 m/s

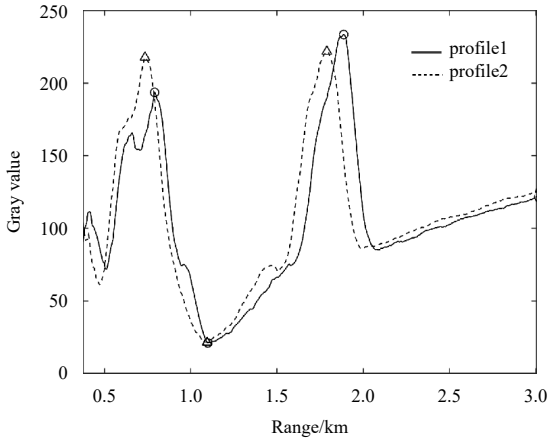

Fig. 15. The radial profiles $\bar{I}_{c1}\left(r,\varphi_{p_2}\right)$ and $\bar{I}_{c2}\left(r,\varphi_{p_2}\right)$ of the adjacent two groups of radar image sequences in the propagation direction $\varphi_{p_2}=270°$ of the ISWs.

which can only estimate the average phase velocity of IWs and cannot obtain the phase velocity of each point on the IWs. A novel method is proposed herein to obtain the phase velocity vector of each point on IWs crest effectively, which is verified using the X-band radar images recorded on an oil platform in the SCS, and the phase velocities estimated by the optical flow-based method are close to those derived from the adjacent radial profiles, as well as the phase velocity of the IWs of the sea area measured by previous studies (Wang et al., 2013; Tang, 2019). Moreover, the proposed method is insensitive to the selection of different reference points; hence, it can reasonably estimate the phase velocit-

ies of different parts of IWs. In future research, experiments with *in-situ* observations of IWs will be performed, and the proposed method will be further evaluated using more data.

References

Alpers W. 1985. Theory of radar imaging of internal waves. Nature, 314(6008): 245–247, doi: 10.1038/314245a0

Badiey M, Wan Lin, Lynch J F. 2016. Statistics of nonlinear internal waves during the shallow water 2006 experiment. Journal of Atmospheric and Oceanic Technology, 33(4): 839–846, doi: 10.1175/JTECH-D-15-0221.1

Briscoe M G. 1975. Preliminary results from the trimoored internal wave experiment (IWEX). Journal of Geophysical Research, 80(27): 3872–3884, doi: 10.1029/JC080i027p03872

Chen Zhongbiao, Zhang Biao, Kudryavtsev V, et al. 2019. Estimation of sea surface current from X-Band marine radar images by cross-spectrum analysis. Remote Sensing, 11(9): 1031, doi: 10.3390/rs11091031

Gong Xiaoliang, Bansmer S. 2015. Horn–Schunck optical flow applied to deformation measurement of a birdlike airfoil. Chinese Journal of Aeronautics, 28(5): 1305–1315, doi: 10.1016/j.cja.2015.07.005

Horn B K P, Schunck B G. 1981. Determining optical flow. Artificial Intelligence, 17(1–3): 185–203, doi: 10.1016/0004-3702(81)90024-2

Huang Xiaodong, Chen Zhaohui, Zhao Wei, et al. 2016. An extreme internal solitary wave event observed in the northern South China Sea. Scientific Reports, 6: 30041, doi: 10.1038/srep30041

Jackson C. 2007. Internal wave detection using the Moderate Resolution Imaging Spectroradiometer (MODIS). Journal of Geophysical Research, 112(C11): C11012, doi: 10.1029/2007JC004220

Jia Tong, Liang Jianjun, Li Xiaoming, et al. 2019. Retrieval of internal solitary wave amplitude in shallow water by tandem spaceborne SAR. Remote Sensing, 11(14): 1706, doi: 10.3390/rs11141706

Jia Tong, Liang Jianjun, Li Qiang, et al. 2021. Generation of shoreward nonlinear internal waves south of the Hainan Island: Synthetic aperture radar observations and numerical simulations. Journal of Geophysical Research: Oceans, 126(6): e2021JC017334

Kropfli R A, Ostrovski L A, Stanton T P, et al. 1999. Relationships between strong internal waves in the coastal zone and their radar and radiometric signatures. Journal of Geophysical Research: Oceans, 104(C2): 3133–3148, doi: 10.1029/98JC02549

Lü Haibin, He Yijun, Shen Hui, et al. 2010. A new method for the estimation of oceanic mixed-layer depth using shipboard X-band radar images. Chinese Journal of Oceanology and Limnology, 28(5): 962–967, doi: 10.1007/s00343-010-9022-5

Li Xiaofeng, Clemente-Colón P, Friedman K S. 2000. Estimating oceanic mixed-layer depth from internal wave evolution observed from radarsat-1 SAR. Johns Hopkins APL Technical Digest, 21(1): 130–135

Liang Jianjun, Li Xiaoming, Sha Jin, et al. 2019. The lifecycle of nonlinear internal waves in the northwestern South China Sea. Journal of Physical Oceanography, 49(8): 2133–2145, doi: 10.1175/JPO-D-18-0231.1

Liu A K, Chang Y S, Hsu M K, et al. 1998. Evolution of nonlinear internal waves in the East and South China Seas. Journal of Geophysical Research: Oceans, 103(C4): 7995–8008, doi: 10.1029/97JC01918

Lund B, Graber H C, Xue Jingshuang, et al. 2013. Analysis of internal wave signatures in marine radar data. IEEE Transactions on Geoscience and Remote Sensing, 51(9): 4840–4852, doi: 10.1109/TGRS.2012.2230635

Ning Jing, Sun Lina, Cui Haiji, et al. 2020. Study on characteristics of internal solitary waves in the Malacca Strait based on Sentinel-1 and GF-3 satellite SAR data. Acta Oceanologica Sinica, 39(5): 151–156, doi: 10.1007/s13131-020-1604-2

Orr M H, Mignerey P C. 2003. Nonlinear internal waves in the South China Sea: Observation of the conversion of depression internal waves to elevation internal waves. Journal of Geophysical Research: Oceans, 108(C3): 3064, doi: 10.1029/2001JC001163

Pan Jiayi, Jay D A. 2009. Dynamic characteristics and horizontal transports of internal solitons generated at the Columbia River plume front. Continental Shelf Research, 29(1): 252–262, doi: 10.1016/j.csr.2008.01.002

Plant W J, Keller W C, Hayes K, et al. 2011. Characteristics of internal waves in the South China Sea observed by a shipboard coherent radar. IEEE Journal of Oceanic Engineering, 36(3): 441–446, doi: 10.1109/JOE.2011.2133030

Ramos R J, Lund B, Graber H C. 2009. Determination of internal wave properties from X-Band radar observations. Ocean Engineering, 36(14): 1039–1047, doi: 10.1016/j.oceaneng.2009.07.004

Sun Lina, Zhang Jie, Meng Junmin. 2019. A study of the spatial-temporal distribution and propagation characteristics of internal waves in the Andaman Sea using MODIS. Acta Oceanologica Sinica, 38(7): 121–128, doi: 10.1007/s13131-019-1449-8

Tang Qixuan. 2019. Research on oceanic internal wave detection and parameter extraction technology based on SAR image (in Chinese) [dissertation]. Harbin: Harbin Engineer University

Wang Juan, Huang Weigen, Yang Jingsong, et al. 2011. The internal waves' distribution of whole South China Sea extracted from ENVISAT and ERS-2 SAR images. In: Proceedings Volume 8175, Remote Sensing of the Ocean, Sea Ice, Coastal Waters, and Large Water Regions 2011. Prague, Czech Republic: SPIE, 411–417

Wang Juan, Huang Weigen, Yang Jingsong, et al. 2013. Study of the propagation direction of the internal waves in the South China Sea using satellite images. Acta Oceanologica Sinica, 32(5): 42–50, doi: 10.1007/s13131-013-0312-6

Watson G, Robinson I S. 1990. A study of internal wave propagation in the strait of gibraltar using shore-based marine radar images. Journal of Physical Oceanography, 20(3): 374–395, doi: 10.1175/1520-0485(1990)020<0374:ASOIWP>2.0.CO;2

Xue Jingshuang, Graber H C, Lund B, et al. 2013. Amplitudes estimation of large internal solitary waves in the mid-atlantic bight using synthetic aperture radar and marine X-Band radar images. IEEE Transactions on Geoscience and Remote Sensing, 51(6): 3250–3258, doi: 10.1109/TGRS.2012.2221467

Yang Jingsong, Huang Weigen, Zhou Changbao, et al. 2001. Simulation study on optimal conditions for internal wave observation by SAR. In: Scanning the Present and Resolving the Future. IEEE 2001 International Geoscience and Remote Sensing Symposium. Sydney, NSW, Australia: IEEE, 3288–3290

Zha Guozhen, He Yijun, Yu Tan, et al. 2012. The force exerted on a cylindrical pile by ocean internal waves derived from nautical X-band radar observations and *in-situ* buoyancy frequency data. Ocean Engineering, 41: 13–20, doi: 10.1016/j.oceaneng.2011.12.014

Zheng Quanan, Yuan Yeli, Klemas V, et al. 2001. Theoretical expression for an ocean internal soliton synthetic aperture radar image and determination of the soliton characteristic half width. Journal of Geophysical Research: Oceans, 106(C12): 31415–31423, doi: 10.1029/2000JC000726

Zhou Liying, Yang Jingsong, Wang Juan, et al. 2016. Spatio-temporal distribution of internal waves in the Andaman Sea based on satellite remote sensing. In: 2016 9th International Congress on Image and Signal Processing, BioMedical Engineering and Informatics (CISP-BMEI). New York: IEEE, 624–628